nature communications

Article | Article in Press

https://doi.org/10.1038/s41467-026-76803-x

Deep carbon cycling drives the splitting of the 520-km mantle discontinuity

Received: 4 December 2025

Accepted: 5 August 2026

Published online: 21 August 2026

Check for updates

Xinyue Zhang[1,2], Wei Wei[1,8], Youyue Zhang[3] ✉, Zhu Mao[1,4] ✉, Ningyu Sun[1], Daoyuan Sun[1,4], Wei Leng[1,4], Takashi Yoshino[2], Izumi Mashino[2], Tomoo Katsura[5], Jiewen Li[6], Wancai Li[1] & Jung-Fu Lin[7]

Carbon cycling into Earth's deep interior regulates melting, redox state, and volatile transport, yet its imprint on mantle seismic structure remains unclear. The sporadic splitting of the 520-km discontinuity, expressed as a secondary reflector near 560 km beneath slabs and mantle upwellings, has been attributed to davemaoite ($CaSiO_3$) exsolution, although its shear-wave properties cannot produce the required 2–4% impedance contrast. We conduct high pressure-temperature experiments (~20 GPa, 1200–1600 °C) to determine how carbonate-altered oceanic crust reorganizes mantle layering. Here we show that carbonate addition drives Ca-Mg exchange with silicates, increases Ca incorporation into silicates under Fe-rich conditions, and enhances davemaoite exsolution. This process yields 12–33(2) vol.% davemaoite near ~ 560 km, sufficient to match impedance contrasts observed. Davemaoite-rich crust could be recycled by mantle plumes, accounting for the 560-km reflector beneath hot regions. Subducted carbonates thus reshape mineral equilibria, reinforce chemical stratification, and generate persistent seismic signatures of deep carbon cycling.

The deep carbon cycle governs the long-term exchange of carbon between Earth's surface and interior, exerting fundamental control on climate stability, volcanic degassing, and planetary habitability[1–3]. Substantial progress has been made in tracing carbon transport within subducting slabs, assessing the stability of carbon-bearing minerals at extreme pressure-temperature (P-T) conditions, and estimating the carbon reservoirs hosted in the transition zone and lower mantle[4–6]. These advances have established carbon as a key volatile in the deep Earth system, yet its role has so far been regarded primarily in terms of mobility, storage, and surface exchange[7–12]. A critical, largely unexplored question is whether subducted carbon can chemically restructure the mantle sufficiently to leave detectable geophysical signatures.

Understanding this possibility requires revisiting the origin of seismic discontinuities. The large-scale structure of the mantle has long been attributed to major silicate phase transitions, which generate the global 410- and 660-km boundaries that partition the mantle into distinct layers[13]. In contrast, smaller-scale features, such as the discontinuity near 520 km, are less well constrained and remain enigmatic[14–17]. In several subduction zones (e.g., North America and Indonesia) and hot regions (e.g., Hawaii and southern Africa), this discontinuity splits into two distinct reflectors, with the secondary one commonly found between 520 and 600 km and most frequently near

[1]Deep Space Exploration Laboratory/School of Earth and Space Sciences, University of Science and Technology of China, Hefei, China. [2]Institute for Planetary Materials, Okayama University, Misasa, Japan. [3]Geodynamics Research Center, Ehime University, Matsuyama, Japan. [4]State Key Laboratory of Precision Geodesy, School of Earth and Space Sciences, University of Science and Technology of China, Hefei, China. [5]Bayerisches Geoinstitut, University of Bayreuth, Bayreuth, Germany. [6]Hubei Subsurface Multi-Scale Imaging Key Laboratory, School of Geophysics and Geomatics, China University of Geosciences, Wuhan, China. [7]Department of Earth and Planetary Sciences, Jackson School of Geosciences, The University of Texas at Austin, Austin, TX, USA. . [8]Present address: Exploration and Development Research Institute, PetroChina Southwest Oil and Gasfield Company, Chengdu, China.
✉e-mail: zhang.youyue.rn@ehime-u.ac.jp; zhumao@ustc.edu.cn

https://doi.org/10.1038/s41467-026-76803-x

560 km (Supplementary Fig. 1)[18–24]. This secondary reflector has been attributed to the davemaoite ($CaSiO_3$) exsolution from Ca-rich garnet in subducted oceanic crust[23,25]. However, recent experimental studies show that the shear wave velocity of davemaoite is 4–16% lower than previously estimated[26–28], reducing the shear-wave impedance contrast ($I_{SS} = \frac{\rho_2 V_{S2} - \rho_1 V_{S1}}{\rho_1 V_{S1}}$) to only 0.5–1.3%, far below the 2–4% required by seismic observations[25,29–34]. This persistent mismatch indicates that classical silicate phase-transition models alone cannot explain the

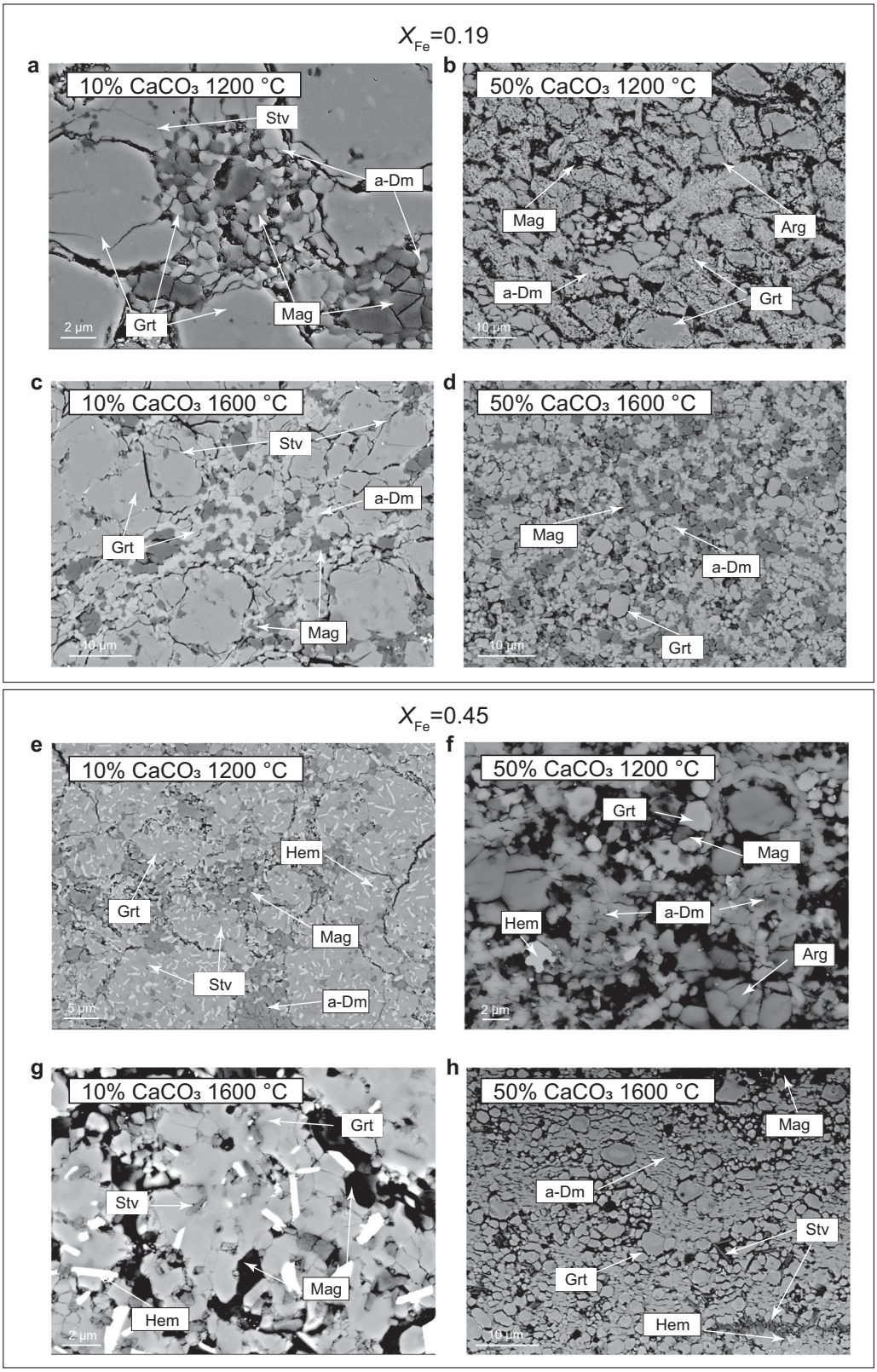

Fig. 1 | Back-scattered electron images of recovered products at 20 GPa and high temperatures. Samples with X_{Fe} = 0.19 in (**a**–**d**), and X_{Fe} = 0.45 in (**e**–**h**). Experimental temperatures are 1200 °C in (**a**, **b**, **e**, **f**), and 1600 °C in (**c**, **d**, **g**, **h**). $CaCO_3$ content is 10 wt.% in (**a**, **c**, **e**, **g**), and 50 wt.% in (**b**, **d**, **f**, **h**).

https://doi.org/10.1038/s41467-026-76803-x

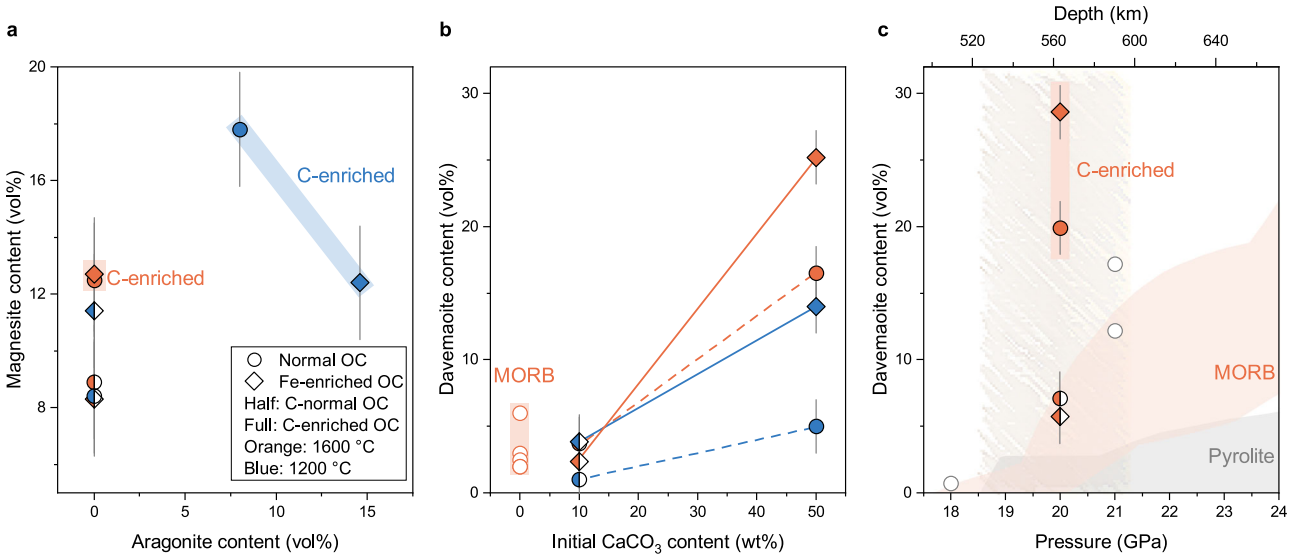

Fig. 2 | Modal abundances of major products after high-pressure experiments. **a** The relationship between magnesite and aragonite content in the products; **b** Davemaoite content in the products with various initial calcium carbonate content. **c** Comparison of exsolved davemaoite content in different compositions. Solid circles: normal oceanic crust with $X_{Fe} = 0.19$; solid diamonds: Fe-enriched oceanic crust with $X_{Fe} = 0.45$; half: C-normal oceanic crust; full: C-enriched oceanic crust; orange: 1600 °C; blue: 1200 °C; open orange circles: previous results for normal oceanic crust[25,29–31,34]; open gray circles: previous results for carbon-enriched pyrolite[79]; lines: linear fitting of our results; thin shaded bands: carbon-enriched system; light shaded areas: amount of exsolved davemaoite in oceanic crust[25,29–31,34] and pyrolitic composition[25,51] from previous studies; thick shaded bands: the apparent depths of 560-km discontinuity[23]. In **c**, the davemaoite content in this study accounts for both our experimental results and the contribution from exsolved davemaoite in average subducted oceanic crust. OC oceanic crust, MORB mid-ocean ridge basalts. Error bars represent one standard deviation.

complexity of mantle layering, and that chemical redistribution, potentially driven by subducted volatiles, must be reconsidered.

To test this hypothesis, we conducted high P-T experiments on mid-ocean ridge basalt (MORB) compositions mixed with varying amounts of $CaCO_3$ under mantle transition-zone conditions. Our results demonstrate that reactions between subducted silicates and $CaCO_3$ drive substantial Ca–Mg exchange, enrich garnet in Ca, and significantly enhance davemaoite exsolution. These phase transformations generate assemblages capable of producing the required 2–4% I_{SS} contrast near ~560 km depth. Our results demonstrate a direct mechanistic link between deep carbon cycling and mantle seismic structure, revealing that subducted carbonates actively reshape mineral equilibria and contribute to the layered architecture of Earth's interior.

Results and discussion

Carbonate-induced Ca-Mg exchange facilitates davemaoite exsolution

High P-T experiments were conducted at 20 GPa (equivalent to ~560-km depth) in a large-volume press to investigate the interaction between basaltic silicates and $CaCO_3$ under conditions relevant to the surface layer of slabs at the bottom mantle transition zone. Temperatures of 1600 °C and 1200 °C were selected to approximate mantle geotherms and typical slab geotherm at this depth, respectively[35,36]. Starting materials of the experiments are silicate glass, which has a relatively low Fe content of $X_{Fe} = 0.19$ [X_{Fe} = Fe/(Fe+Mg +Ca)), Fe is total iron] in subducted oceanic crust[37] (Supplementary Table 1 and Fig. 2). The silicate glass was synthesized with enriched Fe^{3+} contents, consistent with observations of majoritic garnet with 15-87% Fe^{3+} in diamond inclusions from the mantle transition zone and basaltic glass in altered oceanic crust[38–43] (Supplementary Fig. 3). Calcium was excluded from the starting silicate composition and subsequently introduced through $CaCO_3$ with varying proportions (10 and 50 wt.%). These values represent both typical CO_2 concentrations (~4.4 wt.%, carbon-normal condition) within the top 200-500 m of altered oceanic crust[4] and a scenario involving strong carbon enrichment (~22 wt.%, carbon-enriched condition)[44,45]. This experimental design allows a direct assessment of carbonate-silicate reactions under relevant P-T conditions and their dependence on bulk carbon content.

The recovered phase assemblage from high P-T experiments includes garnet, stishovite, magnesite, and amorphous davemaoite (Fig. 1, Supplementary Figs. 4–7, Supplementary Table 2). Garnet, stishovite, and magnesite were identified by X-ray diffraction, while davemaoite could not be resolved due to its rapid vitrification upon quenching and was instead recognized based on its chemical composition and irregular amorphous textures similar to those reported in previous experimental studies (Supplementary Table 2)[30,46,47]. The presence of magnesite [(Mg, Fe)CO_3] rather than Ca-carbonate, indicates that Mg-carbonates are the stable carbonate phase in subducted lithologies at these depths[7,48–50]. This compositional shift reflects a Ca-Mg exchange reaction between carbonate and silicate phases, whereby Ca from Ca-carbonate is incorporated into silicates, and Mg is transferred into the carbonate phase to form stable magnesite phase (Fig. 2a, Supplementary Figs. 6, 7). The overall exchange reaction could be expressed simply as:

$$CaCO_3 + (Mg, Fe) - \text{bearing silicate} \rightarrow (Mg, Fe)CO_3 + (Mg, Fe, Ca) - \text{bearingsilicate}$$

The amount of exsolved davemaoite is primarily dictated by the bulk $CaCO_3$ content, with temperature acting as a secondary modulator (Fig. 2b, Supplementary Table 3). Carbonate-rich systems consistently yield greater davemaoite production, indicating that Ca availability strongly influences Ca-Mg exchange. At 1200 °C, only 1(1) vol.% davemaoite forms in samples containing 10 wt.% initial $CaCO_3$, while $CaCO_3$-enriched assemblages yield up to 5(2) vol.% davemaoite at the same temperature. In $CaCO_3$-enriched systems, aragonite ($CaCO_3$) persists in the reaction products, suggesting that the Ca-Mg exchange remains incomplete under these conditions. Raising the temperature to 1600 °C accelerates the reaction, eliminating residual aragonite even in systems with high initial $CaCO_3$. At this temperature,

https://doi.org/10.1038/s41467-026-76803-x

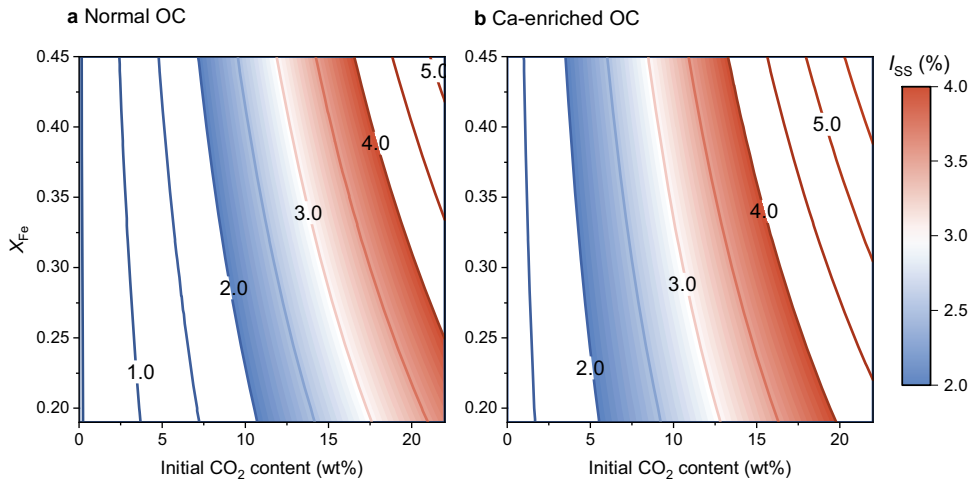

Fig. 3 | Velocity impedance contrast of shear wave in subducted oceanic crust at 20 GPa and 1600 °C. a Oceanic crust (OC) with initial Ca content of $X_{Ca} = 0.38$ (Normal oceanic crust)[29–31,34]. **b** Oceanic crust with a high initial Ca content of $X_{Ca} = 0.48$ (Ca-enriched oceanic crust)[25]. Contour: shear-wave impedance contrast; shaded area: I_{SS} determined by seismic studies[18,23].

samples with 10 wt.% initial $CaCO_3$ produce 4(2) vol.% davemaoite, which is slightly more than the ~3(2) vol.% formed in unaltered MORB compositions at the same depth[29–34]. In $CaCO_3$-rich lithologies with up to 50 wt.% initial $CaCO_3$, davemaoite exsolution can reach 17(2) vol.% under typical mantle geotherms at 560 km depth[36]. Considering that subducted crust also carries additional Ca in silicates, our results suggest that carbonate-altered lithologies could release up to ~7–20(2) vol.% davemaoite at this depth with initial $X_{Ca} = 0.38$ [$X_{Ca} = Ca/(Fe+Mg+Ca)$] (Fig. 2c). If the initial Ca content is as high as shown in Saikia et al.[25] ($X_{Ca} = 0.48$), the exsolved davemaoite from carbon-altered oceanic crust at 560-km depth could be as high as 12–25(2) vol.%. For comparison, the davemaoite exsolved in pyrolite composition is only 0–3 vol.% at this depth[25,51]. These findings establish that carbonate addition, not temperature alone, is the primary driver of Ca-Mg exchange and davemaoite formation in the transition zone.

Iron amplifies carbonate-driven davemaoite formation in carbon-enriched system

In addition to temperature and carbon content, subducted oceanic crust exhibits significant variability in Fe concentration (Supplementary Fig. 2). To assess its effect on davemaoite exsolution, we also conducted experiments using carbonate-altered basaltic compositions with a higher Fe content of $X_{Fe} = 0.45$, as evidenced by East Pacific Rise lavas, at P-T conditions corresponding to 560 km depth[52,53] (Supplementary Fig. 2). In contrast to the results with normal iron content in the system, hematite was observed in the experimental products at both 1200°C and 1600°C (Fig. 1). When the initial $CaCO_3$ content is 10 wt.%, the overall Ca abundance in the system is low. Within the experimental uncertainty, increasing Fe content has little effect on the amount of exsolved davemaoite (Fig. 2b). At 1200 °C, samples with 10 wt.% initial $CaCO_3$ and $X_{Fe} = 0.45$ yield only 4(2) vol.% davemaoite, which is slightly more than that formed in subducted oceanic crust with average-Fe content ($X_{Fe} = 0.19$) and the same $CaCO_3$ content. Increasing the temperature to 1600 °C results in a slight decrease in davemaoite abundance (2(1) vol.%), but this difference falls within experimental uncertainty.

In contrast, in carbon-enriched systems, Fe strongly promotes davemaoite exsolution (Fig. 2b). At 1200 °C, although aragonite remains in the reaction products in the Fe-rich system ($X_{Fe} = 0.45$), indicating incomplete Ca-Mg exchange, the amount of exsolved davemaoite increases to 14(2) vol.%, far exceeding the 5(2) vol.% formed in samples with $X_{Fe} = 0.19$ and the same $CaCO_3$ content. Under Fe ($X_{Fe} = 0.45$) and carbon-rich conditions, raising the temperature to 1600 °C further enhances davemaoite formation, with abundances reaching 25(2) vol.%. Fe enrichment facilitates davemaoite exsolution. Compared with pyrope, Fe-rich garnet decomposes at lower pressures[54,55]. When $CaCO_3$ content is low, and thus little Ca is available to drive Mg-Ca exchange, the influence of Fe is minor, especially given the uncertainty in estimating davemaoite abundance. At higher $CaCO_3$ contents, however, the reduced stability of Fe-rich garnet facilitates Ca transfer from $CaCO_3$ into silicates and promotes more extensive davemaoite exsolution. Considering additional Ca hosted in silicates within subducted crust ($X_{Ca} = 0.38$), our results suggest that Fe- and carbon-enriched oceanic lithologies could exsolve up to 23–29(2) vol.% davemaoite at 560 km depth (Fig. 2c). If the initial Ca content in carbon-altered oceanic crust is also high ($X_{Ca} = 0.45$), the exsolved davemaoite at 560-km depth could be further increased to 28-33(2) vol.%. This highlights that Fe enrichment significantly enhances the effect of carbonate on davemaoite exsolution.

It is worth noting that Fe, Ca, and C are intrinsically coupled in carbonated oceanic crust systems and therefore occur as components of interconnected mineral assemblages rather than as independent variables. Accordingly, the starting compositions used in this study were designed to reproduce the mineralogical and chemical characteristics of natural carbonated oceanic crust. Within this geologically realistic compositional framework, carbonate enrichment increases the availability of Ca for davemaoite formation while simultaneously modifying carbonate–silicate phase relations. The observed variations in davemaoite abundance therefore reflect the integrated response of the system to coupled compositional changes, which is the behavior expected in natural subducted oceanic crust.

Implication

A deep carbon signature in mantle layering. To investigate the origin of the 520-km discontinuity splitting, we constructed a model to evaluate whether carbonate alteration in subducted oceanic crust can drive sufficient davemaoite exsolution to produce the required seismic impedance contrast at 560 km depth. We calculated the I_{SS} induced by davemaoite exsolution across a range of compositional and thermal conditions (Fig. 3, Supplementary Figs. 8, 9, and Supplementary Table 4).

Along a typical mantle geotherm (~1600°C at 560 km)[36], subducted crust with a typical $X_{Ca} = 0.38–0.48$ yields 2–8(2) vol.% davemaoite, resulting in an I_{SS} of 0.5–1.3(1)%, well below the 2–4% range reported by seismic studies[23,37] (Supplementary Fig. 2). Since davemaoite can accommodate a range of substituting elements in

https://doi.org/10.1038/s41467-026-76803-x

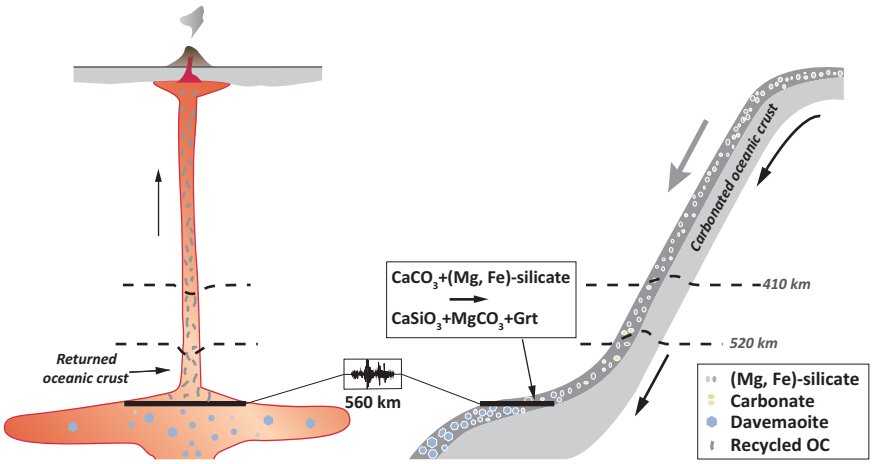

Fig. 4 | Sketch of the formation of 520-km discontinuity splitting. Cartoon shows the proposed mechanism for the splitting of the 520-km discontinuity in the mid-transition zone. $CaCO_3$ reacts with silicates in the carbonated oceanic crust during slab sinking, which greatly increases Ca contents in silicates. The exsolution of davemaoite from the Ca-enriched oceanic crust could be seismically detected to exhibit an I_{SS} of 2–4% at 560-km depth. The upwelling plume could carry the ancient recycled altered oceanic crust back to the Earth's surface with a great Ca content, which could also exhibit a seismic signature of 2–4% *I*ss at ~560-km depth. The transformation of light grey to dark grey means the increase of the amount of Ca in silicate, while the dark yellow to light yellow means the decrease of the amount of Ca in carbonate.

subducted oceanic crust, such as Ti[30,56], here we also calculated the I_{SS} when Ti is present in davemaoite. In subducted oceanic crust, the bulk TiO_2 content is typically ~1.7 wt.%[57]. Given the modeled modal abundance of davemaoite (2–8 vol.%, depending on initial Ca content), Ti is redistributed into the davemaoite reservoir, yielding an estimated substitution level of ~0.21–0.39 per formula unit [$Ca(Ti_{0.21}Si_{0.79})O_3$-$Ca(Ti_{0.39}Si_{0.61})O_3$]. At this level of substitution, the calculated reduction in I_{SS} is 0.3-1.0(1)% for Ti-bearing davemaoite relative to end-member davemaoite of 0.5–1.2(1)%. Therefore, the influence of Ti is small on the I_{SS} of the davemaoite exsolution, and thus is not considered in further modeling.

Our experimental results identify carbonated oceanic crust as a critical supplementary Ca reservoir. The carbonate content of altered oceanic crust is highly heterogeneous and can reach up to ~30 wt% as CO_2 (~68 wt% $CaCO_3$) in its upper 200–500 m[44,45]. Such high initial carbonates abundances enhance the possibility of carbonate to deeper mantle depths[58]. The enrichment of carbonate facilitates Ca-Mg exchange between carbonate and silicate phases upon subduction. This process significantly increases Ca availability in garnet and enhances davemaoite exsolution.

In the modeling, we focus on the first-order effect of davemaoite exsolution on seismic impedance and do not explicitly include the effect of decreasing $CaCO_3$ abundance on I_{SS}. This is because Ca-Mg exchange between carbonates and silicates in subducted oceanic crust is likely not confined to the conditions near 560 km depth observed in our experiments. Instead, this reaction may proceed continuously along the slab's descent, progressively enriching the crust in Ca[48,59]. Some $CaCO_3$ may also decompose at shallower depths, releasing CO_2 or forming diamond before reacting with silicates, while the produced CaO preferentially enters silicate phases[7,10]. In addition, carbonate-bearing phases generally exhibit much lower seismic velocities[11], explicitly coupling carbonate reduction with enhanced davemaoite exsolution would introduce additional contributions that would likely increase the calculated I_{SS} anomaly.

Here, we considered an average initial Ca content of $X_{Ca} = 0.38$ in subducted oceanic crust (Fig. 3a, Supplementary Fig. 2). Linear fits to our experimental constraints suggest that the subducted oceanic crust with an initial CO_2 content of 11 wt.% (25 wt.% $CaCO_3$) and $X_{Fe} = 0.2$ can generate ~12 vol.% davemaoite (Fig. 2b), producing an I_{SS} of 2.0(1)% at 560-km depth and 1600°C. In Fe-rich system ($X_{Fe} = 0.45$), only 8 wt.% CO_2 (~18 wt.% $CaCO_3$) is required to achieve comparable impedance contrasts, reflecting the enhanced efficiency of exsolution in Fe-bearing systems. In carbon-enriched subducted oceanic crust with higher Fe content (22 wt.% CO_2 and $X_{Fe} = 0.45$), davemaoite abundance can reach ~24 vol.% with I_{SS} of 4.0(2)%, fully matching the seismic observation[18,23]. If the subducted oceanic crust has a greater initial Ca content of $X_{Ca} = 0.48$ ($X_{Fe} = 0.19$–0.45)[25], addition of 5–20 wt.% CO_2 is enough to exsolve 12–24 vol.% davemaoite at 560-km depth and generate an I_{SS} of 2.0–4.0(2)% (Fig. 3b).

These results demonstrate that carbonate within subducted lithologies exerts a first-order control on seismic properties at the mantle transition zone (Fig. 4). The carbon transportation in the Earth's deep interior is highly heterogeneous[60]. In regions such as the western Pacific, Indonesia, and Middle East, subducting slabs have transported greater amounts of carbon into Earth's interior than other regions over the past 250 million years[60]. Meanwhile, the prolonged stagnation of slabs within the mantle transition zone (MTZ) in these regions allows sufficient time and heating from the surrounding mantle for extensive carbonate-silicate interaction, calcium redistribution, and davemaoite exsolution[61,62]. Even in non-stagnant slabs that descend along cooler geotherms (~1200 °C), our model predicts that carbonate-rich crusts (>10 wt.% CO_2) can still exsolve 12–24 vol% davemaoite at 560 km depth, yielding an I_{SS} of 2.0–4.0(2)%, in agreement with seismic observations[62] (Supplementary Fig. 9). Consequently, these regions are expected to exhibit relatively large I_{SS} values in seismic observations[23].

Additional support comes from inclusions in superdeep diamonds, where garnet exhibits exceptionally high Ca contents ($X_{Ca} = 0.64$)[63], along with HIMU-like geochemical signatures[64–66] that are widely interpreted as reflecting ancient recycled oceanic crust[67,68]. Upon entering the mantle transition zone, such Ca-rich (davemaoite-bearing) recycled crust is expected to exhibit lower seismic velocities than the surrounding pyrolitic mantle[26,69]. This is consistent with seismic observations of low shear-wave scatterers within hot plumes, which have been interpreted as returning fragments of subducted oceanic crust[70]. The 560-km discontinuity observed beneath mantle plumes may thus reflect the accumulation of these recycled materials, enriched in Ca through deep carbon-silicate interactions.

Importantly, even within plume-related settings, the inferred I_{SS} associated with the ~560-km discontinuity shows strong regional variability. For example, plume systems sampling HIMU-type reservoirs such as Bermuda are characterized by relatively high I_{SS},

consistent with more abundant or better-connected Ca-rich recycled components[23,63]. In contrast, plume regions such as Hawaii exhibit markedly weaker I_{SS}, suggesting more diluted, dispersed, or less coherent expressions of recycled crustal heterogeneities within the upwelling mantle[23,63]. Such spatial variability implies that recycled Ca-bearing materials are not uniformly preserved within plume conduits, but are sampled in different proportions depending on the degree of mixing and entrainment during mantle convection, leading to heterogeneous seismic expression of the ~560-km discontinuity[23].

Taken together, our results establish a direct and quantitative link between deep carbon cycling and mantle seismic structure. The splitting of the 520-km discontinuity arises not solely from thermal or bulk compositional heterogeneity, but from the fate of carbonates preserved in subducting slabs. Far from being a passive component, carbon actively modifies phase equilibria, drives chemical differentiation, and leaves a seismic fingerprint in Earth's deep interior. The 560-km discontinuity thus emerges as a dynamic interface shaped by the redistribution of carbon in Earth's mantle-a seismic signature of the deep carbon cycle itself.

Methods

Sample preparation

Two basaltic starting glass samples with X_{Fe} that represent relatively Fe-poor and Fe-rich endmember compositions within the natural compositional range of subducted oceanic crust, were synthesized from reagent-grade MgO, SiO_2, Al_2O_3, and Fe_2O_3 (Supplementary Fig. 2). Prior to weighing, the oxides were pre-dried to remove adsorbed water: MgO, SiO_2 and Al_2O_3 at 1000°C for 12 h, and Fe_2O_3 at 200 °C in a vacuum furnace for more than one week. The mixtures were homogenized by grinding in an agate mortar with ethanol for 3 h. To produce starting glasses with $Fe^{3+}/\Sigma Fe$ ratios comparable to those inferred for altered oceanic crust and majoritic garnet inclusions from the mantle transition zone, the oxide mixtures were first heated at 1200 °C (iron-rich) and 1300 °C (iron-poor content) for 24 h in a CO_2-H_2 gas mixing furnace under a controlled oxygen fugacity of iron-wustite (IW) + 1 buffer. This treatment produced Fe^{2+}-rich precursor materials. The reduced products were reground for 1 h, and then enclosed in Pt capsules, melted at 1500 °C for 2 h in air, and rapidly quenched in water to produce homogeneous partially oxidized glasses.

The bulk compositions of the quenched glasses were determined using a field-emission electron probe microanalyzer (EPMA; JEOL JXA-8800 at IPM) operated at 15 kV accelerating voltage and a beam current of 1 nA. The Fe-poor glass contains 26.3(1) wt.% MgO, 11.0(2) wt.% FeO, 13.0(1) wt.% Al_2O_3, and 49.4(4) wt.% SiO_2, corresponding to X_{Fe} = 0.19. The Fe-rich glass contains 16.2(3) wt.% MgO, 23.7(3) wt.% FeO, 12.5(2) wt.% Al_2O_3, and 47.0(4) wt.% SiO_2, corresponding to X_{Fe} = 0.45 (Supplementary Table 1 and Fig. 2). These measured glass compositions were used as the effective bulk compositions for all subsequent experiments and modeling. The Fe oxidation state in quenched basaltic glass was determined by energy-domain synchrotron Mössbauer spectroscopy (SMS) at beamline BL11XU, SPring-8[71]. The SMS setup employed a nuclear-resonant monochromator using a $^{57}FeBO_3$ (111) crystal to achieve neV-scale energy resolution. A 2 μm thick α-^{57}Fe foil was used to calibrate the Doppler velocity scales under ambient conditions. The X-ray beam size is approximately 30 × 30 μm. Spectra were collected using a focused beam (~30 × 30 μm) for ~1 h and fitted with pseudo-Voigt line-shape doublets using the MossA software package[72].

The quenched glasses were ground again for 1 h to obtain fine powders. Calcium carbonate powder ($CaCO_3$) was dried at 110 °C for 6 h and then mixed with the basaltic glasses at weight ratios of 1:9 and 5:5 ($CaCO_3$: basalt) for 1 h. The mixtures were subsequently dried in a vacuum furnace at 80 °C before high-pressure experiments.

High-pressure experiments

High-pressure experiments were performed at 20 GPa and 1200-1600 °C for durations of 6-12 hours using a 1000-ton and 5000-ton Kawai-type multi-anvil apparatus at the Institute for Planetary Materials (IPM), Okayama University. The second-stage anvils were F08-grade tungsten carbide (WC) cubes with 4 mm truncations, and Cr-doped MgO octahedra with 10 mm edge length served as the pressure medium. A $LaCrO_3$ cylindrical heater with two lids at both ends was positioned at the center of the octahedron. The starting materials were loaded into gold capsules with 0.5 mm in length and 1.2 mm in outer diameter, which were placed inside MgO sleeves fitted with lids to insulate the sample from the heater. Temperature was monitored using a W97Re3-W75Re25 thermocouple. The samples were first compressed to 6.5 MN, corresponding to a pressure of 20 GPa, before heating to the target temperature. Pressure was calibrated based on the transition from wadsleyite to ringwoodite in Mg_2SiO_4[73] and the transition from akimotoite to bridgmanite[74]. Samples were heated to 1200 °C and held for 12 hours, or to 1600 °C and held for 6 hours, respectively, then quenched by cutting off the power supply. Decompression to ambient pressure was carried out over a period of 12 h.

Sample characterization

Recovered capsules were embedded in epoxy and polished using Al_2O_3-coated sandpaper followed by Al_2O_3 polishing powder to expose the sample surface without introducing additional carbon contamination. Phase identification was conducted using a micro-focus X-ray diffractometer (RINT RAPID II, RIGAKU Co., Japan) equipped with an imaging plate detector at IPM. Measurements were performed with a Cu Kα X-ray source at 40 kV and 30 mA, using a 100 μm collimator. For microstructural and compositional analyses, sample surfaces were coated with Au, Pt, or Ir before scanning electron microscopy (SEM) observation at IPM and University of Science and Technology of China (USTC). Quantitative chemical analyses were performed using EPMA (JEOL JXA-8800 at IPM and JXA-8530F at State Key Laboratory of Lithospheric and Environmental Coevolution, USTC), operating at 15 kV with probe currents of 1 or 5 nA. Compositional mapping was carried out on each capsule using EPMA at IPM with probe currents of 100 nA to quantify modal abundances. The modal proportion was based on the back-scattered electronic images using the ImageJ software[75]. Flank method[76,77] on electron probe is applied to calculate the $Fe^{3+}/\sum Fe$ ratio of garnets in the product of X_{Fe} = 0.19 and 10 wt.% $CaCO_3$ system at 1200°C, which shows that the Fe^{3+} content in garnet is heterogeneous, ranging from 20% to 70% (Supplementary Table 5).

Modeled impedance contrast of the davemaoite exsolution reaction

In this study, we focused on quantifying the effect of davemaoite exsolution on I_{SS}, while excluding the contribution from variations in bulk $CaCO_3$ content to avoid potential overestimation. Phase assemblages and modal proportions were constrained using the experimental results of our four starting compositions, supplemented by interpolation for intermediate compositions. Because the exact compositions of garnet before and after exsolution could not be directly determined from the recovered samples, the amount of consumed $Ca_3Al_2Si_3O_{12}$ garnet was estimated stoichiometrically from the measured davemaoite abundance. We consider the Ca-Mg exchange through:

$$3CaCO_3 + \underbrace{(Mg,Fe)_3(Al,Fe)_2Si_3O_{12}}_{Mg,Fe-garnet} \rightarrow 3(Mg,Fe)CO_3 + \underbrace{(Ca,Mg,Fe)_3(Al,Fe)_2Si_3O_{12}}_{Ca-garnet} \quad (1)$$

This Ca enrichment subsequently promotes the exsolution of davemaoite through reactions such as[25]:

$$Ca_3(Al,Fe)_2Si_3O_{12} + 3/4Mg_4Si_4O_{12} \rightarrow 3CaSiO_3 + Mg_3(Al,Fe)_2Si_3O_{12} \quad (2)$$

We calculated the density, bulk, and shear moduli of individual minerals before and after the davemaoite exsolution reaction at 20 GPa and 1200/1600°C using the literature elasticity data (Supplementary Table 4). The density, bulk and shear moduli of a multiphase assemblage were further computed following[78]:

$$\rho = \sum \rho_i V_i$$
$$M = \frac{1}{2}\left[\sum V_i M_i + \left(\sum V_i M_i^{-1}\right)^{-1}\right] \quad (3)$$

where V_i, ρ_i, M_i are the volume percentage, density, and bulk (shear) modulus of the i^{th} phase, respectively. Sound velocity of a multiphase assemblage is computed following:

$$\rho V_P^2 = K_S + 4G/3$$
$$\rho V_S^2 = G \quad (4)$$

where V_P and V_S are the compressional- and shear-wave velocities, respectively. K_S is the adiabatic bulk modulus, and G is the shear modulus. The impedance contrast across the davemaoite exsolution is:

$$I_{PP} = \frac{\rho_2 V_{P2} - \rho_1 V_{P1}}{\rho_1 V_{P1}}, I_{SS} = \frac{\rho_2 V_{S2} - \rho_1 V_{S1}}{\rho_1 V_{S1}} \quad (5)$$

where I_{PP} and I_{SS} are the compressional- and shear-wave impedance contrast, respectively. Superscript 1 and 2 represent the velocity and density before and after the reaction.

Ca-Mg exchange may also occur at shallower depths as[48]:

$$CaCO_3 + Mg_2Si_2O_6 \rightarrow MgCO_3 + MgCaSi_2O_6 \quad (6)$$

Enstatite Diopside

At greater depths, diopside also transforms into Ca-enriched garnet, leading to elevated Ca contents in garnet compositions in the mantle transition zone. Therefore, regardless of the depth at which the Ca-Mg exchange occurs, it will eventually transform into davemaoite near a depth of ~560 km, and its effect on I_{SS} at this depth is similar to that in our calculations above.

Data availability

All data generated in this study are provided in the article or Supplementary Information. Source data are provided with this paper.

References

1. Farsang, S. et al. Deep carbon cycle constrained by carbonate solubility. *Nat. Commun.* **12**, 4311 (2021).
2. Plank, T. & Manning, C. E. Subducting carbon. *Nature* **574**, 343–352 (2019).
3. Hazen, R. M., Hemley, R. J. & Mangum, A. J. Carbon in Earth's interior: storage, cycling, and life. *Eos Trans. Am. Geophys. Union* **93**, 17–18 (2012).
4. Dasgupta, R. & Hirschmann, M. M. The deep carbon cycle and melting in Earth's interior. *Earth Planet. Sci. Lett.* **298**, 1–13 (2010).
5. Kelemen, P. B. & Manning, C. E. Reevaluating carbon fluxes in subduction zones, what goes down, mostly comes up. *Proc. Natl. Acad. Sci. USA* **112**, E3997–E4006 (2015).
6. Brenker, F. E. et al. Carbonates from the lower part of transition zone or even the lower mantle. *Earth Planet. Sci. Lett.* **260**, 1–9 (2007).
7. Seto, Y., Hamane, D., Nagai, T. & Fujino, K. Fate of carbonates within oceanic plates subducted to the lower mantle, and a possible mechanism of diamond formation. *Phys. Chem. Miner.* **35**, 223–229 (2008).
8. Yoshino, T., Laumonier, M., McIsaac, E. & Katsura, T. Electrical conductivity of basaltic and carbonatite melt-bearing peridotites at high pressures: implications for melt distribution and melt fraction in the upper mantle. *Earth Planet. Sci. Lett.* **295**, 593–602 (2010).
9. Thomson, A. R., Walter, M. J., Kohn, S. C. & Brooker, R. A. Slab melting as a barrier to deep carbon subduction. *Nature* **529**, 76–79 (2016).
10. Tao, R. & Fei, Y. Recycled calcium carbonate is an efficient oxidation agent under deep upper mantle conditions. *Commun. Earth Environ.* **2**, https://doi.org/10.1038/s43247-021-00116-8 (2021).
11. Li, L. et al. Low-velocity structure of subducted oceanic crust in the upper mantle: insights from high pressure and temperature elasticity measurements of aragonite. *J. Geophys. Res. Solid Earth* **128**, https://doi.org/10.1029/2023jb027838 (2023).
12. Yu, Y. et al. Thermal equations of state of magnesite: implication for the complex mid-lower mantle seismic scatterers. *J. Geophys. Res. Solid Earth* **129**, https://doi.org/10.1029/2023jb028026 (2024).
13. Dziewonski, A. M. & Anderson, D. L. Preliminary reference Earth model. *Phys. Earth Planet. Inter.* **25**, 297–356 (1981).
14. Gu, Y., Dziewonski, A. M. & Agee, C. B. Global de-correlation of the topography of transition zone discontinuities. *Earth Planet. Sci. Lett.* **157**, 57–67 (1998).
15. Lawrence, J. F. & Shearer, P. M. Constraining seismic velocity and density for the mantle transition zone with reflected and transmitted waveforms. *Geochem. Geophys. Geosyst.* **7**, https://doi.org/10.1029/2006gc001339 (2006).
16. Julià, J. & Nyblade, A. A. Probing the upper mantle transition zone under Africa with P520s conversions: implications for temperature and composition. *Earth Planet. Sci. Lett.* **368**, 151–162 (2013).
17. Shearer, P. M. Transition zone velocity gradients and the 520-km discontinuity. *J. Geophys. Res. Solid Earth* **101**, 3053–3066 (1996).
18. Deuss, A. & Woodhouse, J. Seismic observations of splitting of the mid-transition zone discontinuity in Earth's mantle. *Science* **294**, 354–357 (2001).
19. Ai, Y. The upper mantle discontinuity structure beneath eastern China. *Geophys. Res. Lett.* **30**, https://doi.org/10.1029/2003gl017678 (2003).
20. Cao, Q., van der Hilst, R. D., de Hoop, M. V. & Shim, S. H. Seismic imaging of transition zone discontinuities suggests hot mantle west of Hawaii. *Science* **332**, 1068–1071 (2011).
21. Tian, Y. et al. Mantle transition zone structure beneath the Changbai volcano: insight into deep slab dehydration and hot upwelling near the 410 km discontinuity. *J. Geophys. Res. Solid Earth* **121**, 5794–5808 (2016).
22. He, C. Evidence for an upwelling mantle plume beneath the Songliao Basin, Northeast China. *Phys. Earth Planet. Inter.* **297**, https://doi.org/10.1016/j.pepi.2019.106316 (2019).
23. Tian, D., Lv, M., Wei, S. S., Dorfman, S. M. & Shearer, P. M. Global variations of Earth's 520- and 560-km discontinuities. *Earth Planet. Sci. Lett.* **552**, https://doi.org/10.1016/j.epsl.2020.116600 (2020).
24. Thomas, C. & Billen, M. I. Mantle transition zone structure along a profile in the SW Pacific: thermal and compositional variations. *Geophys. J. Int.* **176**, 113–125 (2009).
25. Saikia, A., Frost, D. J. & Rubie, D. C. Splitting of the 520-kilometer seismic discontinuity and chemical heterogeneity in the mantle. *Science* **319**, 1515–1518 (2008).
26. Gréaux, S. et al. Sound velocity of $CaSiO_3$ perovskite suggests the presence of basaltic crust in the Earth's lower mantle. *Nature* **565**, 218–221 (2019).

27. Thomson, A. R. et al. Seismic velocities of $CaSiO_3$ perovskite can explain LLSVPs in Earth's lower mantle. *Nature* **572**, 643–647 (2019).
28. Yu, Y. et al. Davemaoite elasticity reveals slab-induced heterogeneity in the mantle transition zone. *Geophys. Res. Lett.* **53**, https://doi.org/10.1029/2025gl118147 (2026).
29. Litasov, K. D. & Ohtani, E. Phase relations in hydrous MORB at 18–28 GPa: implications for heterogeneity of the lower mantle. *Phys. Earth Planet. Inter.* **150**, 239–263 (2005).
30. Ishii, T., Kojitani, H. & Akaogi, M. Phase relations of Harzburgite and MORB up to the uppermost lower mantle conditions: precise comparison with pyrolite by multisample cell high-pressure experiments with implication to dynamics of subducted slabs. *J. Geophys. Res. Solid Earth* **124**, 3491–3507 (2019).
31. Irifune, T. & Ringwood, A. E. Phase transformations in subducted oceanic crust and buoyancy relationships at depths of 600–800 km in the mantle. *Earth Planet. Sci. Lett.* **117**, 101–110 (1993).
32. Ono, S., Ito, E. & Katsura, T. Mineralogy of subducted basaltic crust (MORB) from 25 to 37 GPa, and chemical heterogeneity of the lower mantle. *Earth Planet. Sci. Lett.* **190**, 57–63 (2001).
33. Perrillat, J.-P. et al. Phase transformations of subducted basaltic crust in the upmost lower mantle. *Phys. Earth Planet. Inter.* **157**, 139–149 (2006).
34. Sanehira, T. et al. Density profiles of pyrolite and MORB compositions across the 660 km seismic discontinuity. *High. Press. Res.* **28**, 335–349 (2008).
35. Thompson, A. B. Water in the Earth's upper mantle. *Nature* **358**, 295–302 (1992).
36. Katsura, T. A revised adiabatic temperature profile for the mantle. *J. Geophys. Res. Solid Earth* **127**, https://doi.org/10.1029/2021jb023562 (2022).
37. Stracke, A., Willig, M., Genske, F., Béguelin, P. & Todd, E. (GRO.-data, 2022).
38. Xu, C. et al. Recovery of an oxidized majorite inclusion from Earth's deep asthenosphere. *Sci. Adv.* **3**, e1601589 (2017).
39. Brounce, M., Cottrell, E. & Kelley, K. A. The redox budget of the Mariana subduction zone. *Earth Planet. Sci. Lett.* **528**, https://doi.org/10.1016/j.epsl.2019.115859 (2019).
40. Pan, F. et al. Iron disproportionation in peridotite fragments from the mantle transition zone. *Nat. Commun.* **16**, 5440 (2025).
41. McCammon, C., Hutchison, M. & Harris, J. Ferric iron content of mineral inclusions in diamonds from São Luiz: a view into the lower mantle. *Science* **278**, 434–436 (1997).
42. Kiseeva, E. S. et al. Oxidized iron in garnets from the mantle transition zone. *Nat. Geosci.* **11**, 144–147 (2018).
43. Bach, W. & Edwards, K. J. Iron and sulfide oxidation within the basaltic ocean crust: implications for chemolithoautotrophic microbial biomass production. *Geochim. Cosmochim. Acta.* **67**, 3871–3887 (2003).
44. Chen, C., Forster, M. W., Foley, S. F. & Shcheka, S. S. Carbonate-rich crust subduction drives the deep carbon and chlorine cycles. *Nature* **620**, 576–581 (2023).
45. Staudigel, H., Plank, T., White, B. & Schmincke, H.-U. Geochemical fluxes during seafloor alteration of the basaltic upper oceanic crust: DSDP Sites 417 and 418. *Geophys. Monogr.* **96**, 19–38 (1996).
46. Tschauner, O. et al. Discovery of davemaoite, $CaSiO_3$-perovskite, as a mineral from the lower mantle. *Science* **374**, 891–894 (2021).
47. Irifune, T. Absence of an aluminous phase in the upper part of the Earth's lower mantle. *Nature* **370**, 131–133 (1994).
48. Kushiro, I. Carbonate-silicate reactions at high presures and possible presence of dolomite and magnesite in the upper mantle. *Earth Planet. Sci. Lett.* **28**, 116–120 (1975).
49. Zhang, Z., Mao, Z., Liu, X., Zhang, Y. & Brodholt, J. Stability and reactions of $CaCO_3$ polymorphs in the Earth's deep mantle. *J. Geophys. Res. Solid Earth* **123**, 6491–6500 (2018).
50. Lv, M. et al. Reversal of carbonate-silicate cation exchange in cold slabs in Earth's lower mantle. *Nat. Commun.* **12**, https://doi.org/10.1038/s41467-021-21761-9 (2021).
51. Ishii, T., Kojitani, H. & Akaogi, M. Phase relations and mineral chemistry in pyrolitic mantle at 1600–2200 °C under pressures up to the uppermost lower mantle: phase transitions around the 660-km discontinuity and dynamics of upwelling hot plumes. *Phys. Earth Planet. Inter.* **274**, 127–137 (2018).
52. Regelous, M. et al. Variations in the geochemistry of magmatism on the East Pacific Rise at 10°30′N since 800 ka. *Earth Planet. Sci. Lett.* **168**, 45–63 (1999).
53. Wanless, V. D., Perfit, M. R., Ridley, W. I. & Klein, E. Dacite petrogenesis on mid-ocean ridges: evidence for oceanic crustal melting and assimilation. *J. Petrol.* **51**, 2377–2410 (2010).
54. Akaogi, M., Ohmura, N. & Suzuki, T. High-pressure dissociation of $Fe_3Al_2Si_3O_{12}$ garnet: phase boundary determined by phase equilibrium experiments and calorimetry. *Phys. Earth Planet. Inter.* **106**, 103–113 (1998).
55. Liu, Z. et al. Phase relations in the system $MgSiO_3$-Al_2O_3 up to 2300 K at lower mantle pressures. *J. Geophys. Res. Solid Earth* **122**, 7775–7788 (2017).
56. Ishii, T. et al. High pressure-temperature phase relations of basaltic crust up to mid-mantle conditions. *Earth Planet. Sci. Lett.* **584**, https://doi.org/10.1016/j.epsl.2022.117472 (2022).
57. Gale, A., Dalton, C. A., Langmuir, C. H., Su, Y. & Schilling, J.-G. The mean composition of ocean ridge basalts. *Geochem. Geophys. Geosyst.* **14**, 489–518 (2013).
58. Guo, Z. et al. Petrological and thermodynamic constraints on carbonate stability in altered oceanic crust subducted to subarc depths: insights from carbonate-bearing eclogites in the Western Alps. *Geochim. Cosmochim. Acta.* **405**, 205–228 (2025).
59. Biellmann, C., Gillet, P., Guyot, F. O., Peyronneau, J. & Reynard, B. Experimental evidence for carbonate stability in the Earth's lower mantle. *Earth Planet. Sci. Lett.* **118**, 31–41 (1993).
60. Muller, R. D. et al. Evolution of Earth's tectonic carbon conveyor belt. *Nature* **605**, 629–639 (2022).
61. Fukao, Y., Obayashi, M. & Nakakuki, T. Stagnant slab: a review. *Annu. Rev. Earth Planet. Sci.* **37**, 19–46 (2009).
62. Goes, S., Agrusta, R., van Hunen, J. & Garel, F. Subduction-transition zone interaction: a review. *Geosphere* **13**, 644–664 (2017).
63. Huang, S. et al. HIMU geochemical signature originating from the transition zone. *Earth Planet. Sci. Lett.* **542**, https://doi.org/10.1016/j.epsl.2020.116323 (2020).
64. Weiss, Y., Class, C., Goldstein, S. L. & Hanyu, T. Key new pieces of the HIMU puzzle from olivines and diamond inclusions. *Nature* **537**, 666–670 (2016).
65. Castillo, P. R. The recycling of marine carbonates and sources of HIMU and FOZO ocean island basalts. *Lithos* **216-217**, 254–263 (2015).
66. Mazza, S. E. et al. Sampling the volatile-rich transition zone beneath Bermuda. *Nature* **569**, 398–403 (2019).
67. Chauvel, C., Hofmann, A. W. & Vidal, P. HIMU-EM: the French Polynesian connection. *Earth Planet. Sci. Lett.* **110**, 99–119 (1992).
68. Chen, L. et al. Recycled oceanic gabbro produced the depleted component in hotspot magma from the Comei large igneous province in the Kerguelen mantle plume. *Commun. Earth Environ.* **6**, https://doi.org/10.1038/s43247-025-02353-7 (2025).
69. Wei, W., Mao, Z., Sun, N., Sun, D. & Tkachev, S. N. High pressure-temperature single-crystal elasticity of grossular: implications for the low-velocity layer in the bottom transition zone. *Geophys. Res. Lett.* **48**, https://doi.org/10.1029/2021gl093540 (2021).
70. Kaneshima, S. Mid-mantle seismic scatterers beneath the Samoan hotspot. *Phys. Earth Planet. Inter.* **340**, https://doi.org/10.1016/j.pepi.2023.107034 (2023).

71. Mitsui, T. et al. Development of an energy-domain ^{57}Fe-Mossbauer spectrometer using synchrotron radiation and its application to ultrahigh-pressure studies with a diamond anvil cell. *J. Synchrotron Radiat.* **16**, 723–729 (2009).
72. Prescher, C., McCammon, C. & Dubrovinsky, L. MossA: a program for analyzing energy-domain Mössbauer spectra from conventional and synchrotron sources. *J. Appl. Crystallogr.* **45**, 329–331 (2012).
73. Tsujino, N. et al. Phase transition of wadsleyite-ringwoodite in the Mg_2SiO_4-Fe_2SiO_4 system. *Am. Mineral.* **104**, 588–594 (2019).
74. Chanyshev, A. et al. Depressed 660-km discontinuity caused by akimotoite-bridgmanite transition. *Nature* **601**, 69–73 (2022).
75. Rueden, C. T. et al. ImageJ2: ImageJ for the next generation of scientific image data. *BMC Bioinforma.* **18**, 1–26 (2017).
76. Tao, R., Fei, Y., Bullock, E. S., Xu, C. & Zhang, L. Experimental investigation of Fe^{3+}-rich majoritic garnet and its effect on majorite geobarometer. *Geochim. Cosmochim. Acta* **225**, 1–16 (2018).
77. Hofer, H. E. & Brey, G. P. The iron oxidation state of garnet by electron microprobe: Its determination with the flank method combined with major-element analysis. *Am. Mineral.* **92**, 873–885 (2007).
78. Cottaar, S., Heister, T., Rose, I. & Unterborn, C. BurnMan: a lower mantle mineral physics toolkit. *Geochem. Geophys. Geosyst.* **15**, 1164–1179 (2014).
79. Gao, M., Wang, Y., Foley, S. F. & Xu, Y. G. Variable mantle redox states driven by deeply subducted carbon. *Sci. Adv.* **11**, eadu4985 (2025).

Acknowledgements

We thank N.M. Kondo at IPM and T. Xiao at USTC for EPMA measurement, T. Ishii, J. He, and J. Zhu at IPM for high-pressure experiment preparation, X. Gao and Q. Hou at USTC for SEM observation. This work was partially carried out at Instruments Center for Physical Science, University of Science and Technology of China. This study was performed using joint-use facilities of the Institute for Planetary Materials, Okayama University.

Author contributions

Z.M. conceived and supervised the project. Y.Z. designed the experiments. X.Z. conducted the high-pressure experiments and subsequent analyses. Y.Z. and T.Y. directed the experiments and analyses. W. Li assisted with the EPMA measurements and data analysis. I.M. performed the synchrotron Mössbauer spectroscopy measurement. X.Z., W.W., and Z.M. built the models. N.S., T.K., and J.-F.L. contributed to the interpretation of the geophysical implications. D.S. and J.L. contributed to the preparation of the figures and the interpretation of seismology. W. Leng contributed to the geodynamic interpretation. X.Z. wrote the original draft of the manuscript. All the authors discussed the results and revised the manuscript.

Funding

This work was funded by the National Science Foundation of China (42488101 and 42425202), National Key R&D Program of China (2023YFF0803200), and PRIUS Project 2025-A18 at Ehime University to Z.M., by JSPS KAKENHI Grant, JP21H04996 to T.Y., 24K17148 to Y.Z., and by the Joint Use Program at IPM (Project Number I23-013) and Program of China Scholarship Council (No. 202306340150) to X.Z. The Mössbauer measurements were supported by the QST Advanced Research Infrastructure for Materials and Nanotechnology under the remit of "Advanced Research Infrastructure for Materials and Nanotechnology" of the Ministry of Education, Culture, Sports, Science and Technology (MEXT), Japan (QST proposals no. JPMXP1224QS0103, JASRI proposals no. 2024B3584).

Competing interests

The authors declare no competing interests.

Additional information

Supplementary information The online version contains supplementary material available at https://doi.org/10.1038/s41467-026-76803-x.

Correspondence and requests for materials should be addressed to Youyue Zhang or Zhu Mao.

Peer review information *Nature Communications* thanks Sibo Chen and the other, anonymous, reviewer(s) for their contribution to the peer review of this work. A peer review file is available.